RSC Advances

PAPER

View Article Online
View Journal | View Issue



Cite this: *RSC Adv.*, 2025, **15**, 27238

# Effect of various parameters on the morphology of anodic $WO_3$ nanostructure: transition from nanoflowers to nanosheets

Rizwana Ghazi, [a] Habib Ullah,[b] Zia ur Rehman, *[a] Maaz Khan, [c] Sajid Iqbal, [d] Jong-Il Yun, [d] Sung Oh Cho, [d] Sarhang Hayyas Mohammed[ef] and Ghafar Ali *[c]

Received 4th June 2025
Accepted 24th July 2025

DOI: 10.1039/d5ra03947a

rsc.li/rsc-advances

Nanomaterials with diverse morphologies have attracted considerable attention owing to their applications in numerous scientific disciplines. This study investigated the influence of various experimental parameters on the morphology of anodic $WO_3$ nanostructures obtained in aqueous $HNO_3$. X-ray diffraction (XRD) analysis confirmed that $WO_3$ comprises a monoclinic phase, while field-emission scanning electron microscope (FE-SEM) results revealed the formation of $WO_3$ nanoflowers and nanosheets morphologies under optimized conditions. X-ray photoelectron spectroscopy (XPS) analysis further verified the chemical composition and oxidation state ($W^{6+}$) of the $WO_3$ nanoflowers. The proposed mechanism for the formation of nanoflowers and its transition to nanosheets based on chemical reactions is also elucidated. This study provides information regarding the specified parameters and their potential impact on the morphology of the anodic $WO_3$ nanostructures.

## Introduction

In recent years, nanomaterials have attracted considerable attention due to their unique properties and diverse applications. Their physicochemical characteristics are highly dependent on size and morphology, making structural control essential for optimal performance in various fields.[1] Different strategies have been developed for the synthesis of nanomaterials such as co-precipitation,[2] micro-emulsion,[3] hydrothermal,[4] sonochemical,[5] anodization,[1] and sol–gel,[6] *etc.* However, most of these methods are time consuming, complicated, and require special conditions or expensive precursors. Anodization is an electrochemical method that is facile, cost-effective, rapid, and environmentally friendly. This process is generally used for the formation of an oxide layer directly on the surface of a metal substrate with controlled morphology using different electrolytes.[7]

Anodic nanostructures have been widely utilized in diverse applications like corrosion resistance,[8] sensors,[9] lithium-ion batteries (LiBs),[10] solar cells,[11] and supercapacitors[12] *etc.* The formation of anodized aluminum oxide dates back to 1953, as first reported by Keller *et al.*[13] Since then, numerous metals such as titanium,[14] zinc,[15] niobium,[16] nickel,[17] tungsten,[18] and zirconium[19] *etc.*, have been explored. Among transition metal-oxides (TMO), tungsten oxide ($WO_3$) stands out as a wide bandgap (2.6–3.5 eV) semiconductor, gaining significant attention for its applications in electrochemical sensing, photocatalysis, energy storage, electrochromic devices, and the hydrogen evolution reaction (HER).[20–22]

Porous tungsten oxide was reported for the first time by Mukherjee *et al.* (2003)[23] using galvanostatic anodization in 0.2 M oxalic acid. Since then, various electrolytes such as $H_2SO_4$,[24] NaF,[25] HF,[26] $NH_4NO_3$,[27] $Na_2SO_4$,[28] and $H_3PO_4$ (ref. 29) have been successfully used for the synthesis of anodic $WO_3$ with a nanoporous morphology. Similarly, $HNO_3$ has been shown to produce nanosheet-like structures when magnetron sputtered tungsten thin film was anodized.[30] Moreover, Widenkvist *et al.*[31] immersed the tungsten sheet in nitric acid solution at elevated temperature for 3 hours, resulting in the formation of plate-like nanostructures. However, this method is time-consuming compared with anodization.

The anodic oxide layer formed on the tungsten substrate offers several advantages, such as strong adhesion to the metal substrate, which enhances the charge transport. It can also be utilized directly in various applications without any further processing and is cost-effective and time efficient. Moreover, it prevents further oxidation and protects metal from corrosion when exposed to harsh environments. The morphology of the anodic oxide layer can be tailored by adjusting certain parameters such as the applied voltage (controlling the nanostructure

[a]*Department of Chemistry, Quaid-i-Azam University, Islamabad 45320, Pakistan. E-mail: zrehman@qau.edu.pk*

[b]*State Key Laboratory of Silicate Materials for Architectures, Wuhan University of Technology, No. 122, Luoshi Road, Wuhan 430070, China*

[c]*Nanomaterials Research Group (NRG), Physics Division, PINSTECH, Nilore, Islamabad, Pakistan. E-mail: ghafarali@kaist.ac.kr*

[d]*Department of Nuclear and Quantum Engineering (NQe), Korea Advanced Institute of Science and Technology (KAIST), Daejeon 34141, Republic of Korea*

[e]*Department of Pharmacy, College of Pharmacy, Knowledge University, Erbil, Iraq*

[f]*Department of Pharmacy, Al-Kitab University, Altun Kupri, Iraq*

size), reaction duration (affecting thickness), and electrolyte type/concentration. All of these parameters play an important role in tuning the morphology of metal-oxide nanostructure and obtaining the morphology of interest suitable for certain applications.

Given the limited research done on the formation of $WO_3$ nanostructures in $HNO_3$, this study undertakes a comprehensive investigation into the synthesis of $WO_3$ nanostructures, with a particular emphasis on their morphological transition from nanoflowers to nanosheets. The primary objective of this research is to examine the influence of experimental conditions on the structural characteristics of anodic $WO_3$ nanostructures. These conditions are pivotal for synthesizing anodic $WO_3$ nanostructures with desired morphology and properties, including size dimensions, nanostructure density distribution, and layer thickness. To the best of our knowledge, no comprehensive study on the optimization of $WO_3$ using a nitric acid electrolyte has been previously reported. Consequently, this study offers valuable insights for new researchers in this field.

## Experimental

### Synthesis of $WO_3$ nanoflowers

For anodization, tungsten (W) sheets with a thickness of 0.1 mm and purity of 99.99% (Goodfellow, England, UK) were used. Before anodization, the sheets were subjected to a sequential cleaning process involving 5 min of sonication in acetone, ethanol, and deionized water. A two-electrode system was employed for anodization with a Cu rod serving as the counter electrode and a W sheet as the working electrode (anode). Experiments were conducted using a DC power supply (ES015-10, Delta Elektronika, Netherland). The tungsten sheets were anodized at constant voltage (15 V) under various conditions, including temperature (50, 70, and 90 °C), anodizing time (15, 60, and 90 min), and electrolyte molarity (0.5, 1.5, and 3 M). Temperature of the electrochemical setup was controlled using a temperature-controlled digital water bath system. The optimized experiments were performed for 15 min in 40 mL of 1.5 M aqueous $HNO_3$ solution at 15 V. Among the various experiments, a 15 min anodizing duration was found to be optimal for the formation of homogeneous nanoflowers; thus, subsequent experiments were conducted at a constant voltage of 15 V for 15 min. The effects of molarity and temperature were also investigated while keeping the other anodizing parameters fixed. The samples were rinsed with deionized water, dried in an oven at 70 °C for 2 hours, and annealed at 450 °C for 1 hour.[32]

### Characterizations

The surface morphology and elemental composition of the samples were analyzed using field-emission scanning electron microscope (FE-SEM, JSM-IT800, JEOL, Japan) coupled with energy-dispersive X-ray spectroscopy (EDX). The crystal structure and phase purity were examined using X-ray diffraction (XRD) with a SmartLab X-ray diffractometer equipped with a HyPix 3000 detector (Rigaku, Japan), utilizing Cu Kα1 radiation ($\lambda = 1.54056$ Å). X-ray photoelectron spectroscopy (XPS) was employed to investigate the structural properties and oxidation states using a VG Physical Electronics Quantum 2000 scanning ESCA microprobe (Thermo VG Scientific, USA) with Al-Kα radiation as the excitation source.

## Results and discussion

The XPS spectra of the annealed $WO_3$ nanostructure (Fig. 1) displayed all the characteristic peaks of $WO_3$ in both the survey as well as the high-resolution scan. The survey spectrum of $WO_3$ (Fig. 1a) shows peaks corresponding to W 4f, O 1s, and C 1s. The peak for W 4f at approximately 35.2 eV is identified as W $4f_{7/2}$, while the peak around 37.4 eV corresponds to W $4f_{5/2}$ (Fig. 1b), confirming the presence of $W^{6+}$ species coordinated with oxygen in the $WO_3$ lattice. The deconvoluted peak at 284.45 eV represents the C 1s peak for non-oxidized state such as C–C/C–H bonds, while the peak at around 286.5 eV refers to oxidized carbon as in C–O. Both the C 1s peaks are attributed to the XPS system during analysis (Fig. 1c). Moreover, the high-resolution O 1s spectrum (Fig. 1d) shows a main peak at approximately 530.5 eV, corresponding to the W–O bond within the $WO_3$ lattice while the deconvoluted peak at 31.6 eV represents the surface adsorbed oxygen. The XPS results confirm the formation of a highly pure $WO_3$ nanostructure through anodization.

The prepared pristine $WO_3$ nanostructure is amorphous in nature as shown in the XRD pattern (Fig. 2a), which transformed into a crystalline form after annealing at 450 °C, as evidenced by prominent diffraction peaks at 23.27°, 24.33°, 26.45°, 28.90°, 33.28°, 34.07°, 47.7°, 50°, and 53.92° (Fig. 2b). These peaks correspond to the monoclinic crystal structure of $WO_3$, which is characterized by lattice parameters $a = 7.297$ Å, $b = 7.539$ Å, and $c = 7.688$ Å. They aligned with reflections from the crystal planes (020), (200), (120), (112), (022), (202), (004), (140), and (240), as per ICCD # 43-1035. The diffractogram confirms the successful synthesis of pure monoclinic $WO_3$. The sharp and intense peaks indicate good crystallinity after annealing process. The XRD results are corroborated by the XPS analyses.

### Effect of different anodizing parameters on $WO_3$ nanostructure morphology

Anodizing parameters are important for tuning the morphology of anodic nanostructures. From our preliminary experiments, we reach the conclusion that at room temperature, as depicted in the SEM image (Fig. 3a), there is no formation of $WO_3$ nanosheets/nanoflowers. However, the surface is composed of a shallow which decreased owing to the loss of porous oxide layer, as confirmed by the elemental analysis shown in EDX spectrum (Fig. 3b). This is because $HNO_3$ is an inorganic acid which is not reactive at room or very low temperature, and the dissolution of tungsten metal occurs only at high temperature; hence, no specific morphology is obtained at room temperature.[18] Therefore, anodization was performed at 50, 70, and 90 °C to comprehensively study the temperature effect on its morphology.

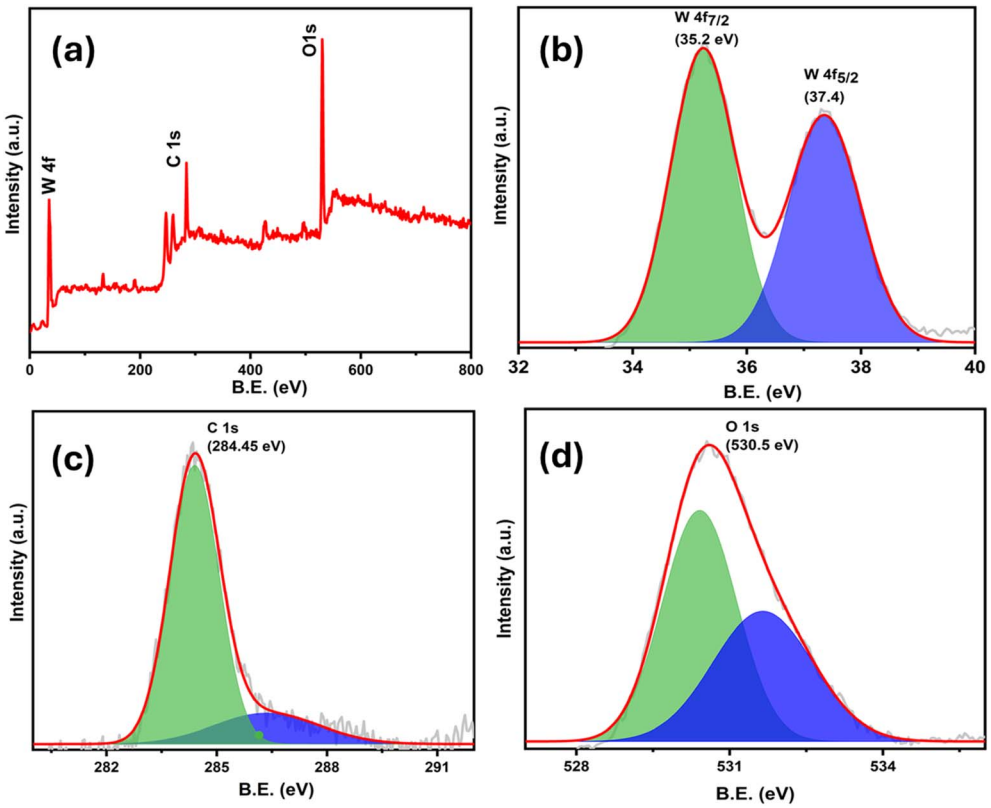


Fig. 1 (a) XPS survey spectrum of the $WO_3$ nanostructure and high-resolution XPS spectra of (b) W 4f, (c) C 1s (d) O 1s.

**Temperature effect**

Fig. 4a–c shows the FESEM images of the pristine anodic $WO_3$ nanostructure obtained at different temperatures (50, 70, and 90 °C). The formation of irregular and dense $WO_3$ nanoflowers is evident from Fig. 4a when anodization was conducted at 50 °C, in contrast to the shallow nanoporous morphology obtained at room temperature (Fig. 3a). As the anodization temperature increased from room temperature to 50 °C, the dissolution of W sheet started which resulted in the formation of nanoflowers with irregular shape morphology. These nanoflowers are comparatively less smooth and entangled (Fig. 4a). A further increase in the anodizing temperature up to 70 °C caused the transition from nanoflowers to regularly stacked nanosheets owing to the detachment of the nanopetals from the nanoflowers and their conversion into a more regular and smoother plate-like morphology. The density and size of the nanosheets were also enhanced owing to the increase in the nucleation and growth rates, which probably occurred in our case with an increase in temperature (Fig. 4b). A similar phenomenon was observed when the temperature was further increased to 90 °C (Fig. 4c) which can be attributed to the Ostwald ripening effect

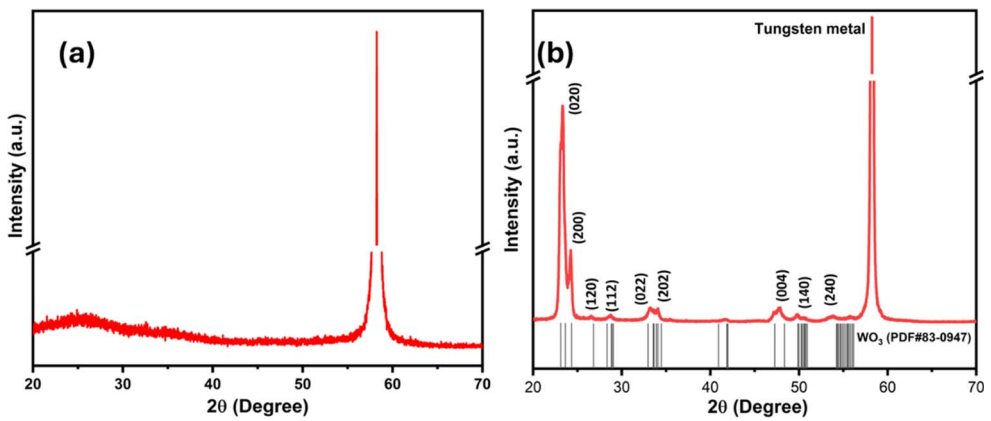


Fig. 2 Diffractogram of pristine (a) and $WO_3$ nanostructure annealed at 450 °C for 1 hour in air (b).

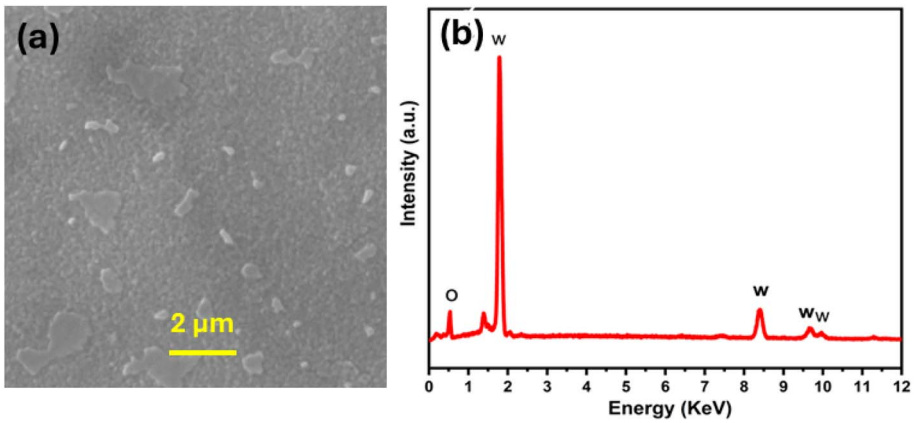


Fig. 3 Top-surface FESEM image of $WO_3$ with shallow nanoporous structure anodized at room temperature (a) and the corresponding EDX spectrum (b).

because increases in temperature expedite the dissolution of small sheets, resulting in the formation of fewer but larger stable sheet-like morphologies, as shown in Fig. 4c.[33] Based on the above observations, 90 °C was found to be the optimum temperature for the formation of $WO_3$ nanosheets and was further used to study the effect of the remaining parameters.

Fig. 4d–f depicted the FESEM images of the samples annealed at 450 °C for 1 hour in air. It can be observed that annealing didn't destroy the morphology of the pristine $WO_3$ nanostructures, except size of the nanosheets, which decreased owing to the loss of adsorbed water during thermal treatment.

### Anodizing time effect

In addition to temperature, the anodization time also played a key role in controlling the morphology of the $WO_3$ nanostructures anodized in 1.5 M $HNO_3$ at 15 V and 90 °C. Homogeneous nanoflowers with regular and smooth shapes were obtained when the tungsten sheet was anodized for 15 min, as shown in Fig. 5a. Ostwald ripening phenomenon can be clearly observed when the anodization time increases from 15 min to 30 min and then to 60 min, as shown in Fig. 5b and c, respectively. As the anodization time increased, the entangled petals of the nanoflowers started to be disentangled, followed by regrowth over the larger petals. When the time was increased to 30 min, the smoothness was lost, as shown in the inset of Fig. 5b, and there was an overall volume expansion due to the dis-entanglement of the nanoflower petals/sheets, as depicted in the low magnification SEM image (Fig. 5b). When the anodizing time was further increased to 60 min, the maximum dissolution of the small sheets was achieved, and the

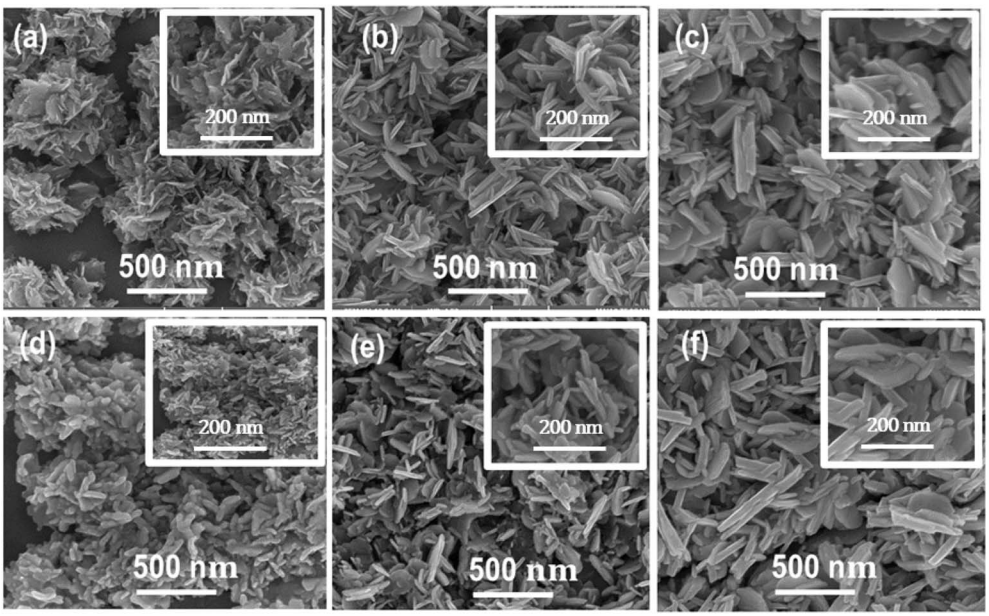


Fig. 4 FSEM images (a–c) of the top surfaces of the as-anodized $WO_3$ nanostructures obtained at 15 V for 15 min at (a) 50, (b) 70, and (c) 90 °C, whereas the FESEM images of the respective annealed samples are given (d–f). The inset shows the respective high-magnification images.

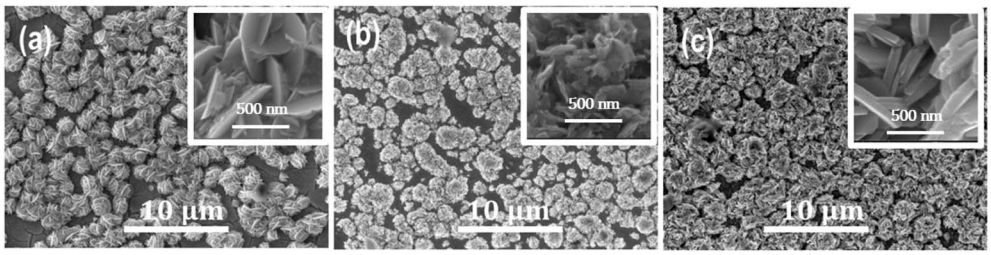


Fig. 5 Top surface FESEM morphology of $WO_3$ nanoflowers obtained in 1.5 M $HNO_3$ at 15 V, and 90 °C at different anodization duration (a) 15 min, (b) 30 min, and (c) 60 min with high magnification images in the inset.

nanosheets had smooth edges with relatively larger sizes and greater thicknesses, as shown in the inset of Fig. 5c. As we were interested in the nanoflowers morphology, therefore 15 min was used in the rest of the experiments as the anodization time.

### Electrolyte molarity effect

Fig. 6 shows FESEM images of $WO_3$ nanostructures anodized at different $HNO_3$ concentrations at a constant temperature and potential. It can be clearly observed from the images that the concentration is mainly associated with the nucleation rate of the nanosheets. After anodizing in 0.5 M $HNO_3$, as shown in Fig. 6a, the density of the nanoflowers was much lower, and most of the surface of the oxide layer was empty/bare, possibly because of the slow nucleation rate due to the low electrolyte concentration. However, when the concentration was increased to 1.5 M and then to 3.0 M, the obvious increase in the reaction kinetics and nucleation resulted in an increase in the density of nanoflowers with their conversion to nanosheets (Fig. 6b and c).

### Magnetic stirring effect

We also studied the effect of magnetic stirring on the morphology of the $WO_3$ nanostructures. An anodization experiment was conducted under continuous stirring while keeping all the other conditions constant for comparison. FESEM images of the $WO_3$ nanostructures obtained with and without stirring are depicted in Fig. 7. As shown in Fig. 7a, without stirring, the nanosheets were much thicker and longer in size than those formed under stirring conditions. We believe that with stirring and, consequently, fast ionic movement, the nanosheets do not have enough time to grow; therefore, dense nanosheets with small sizes can be observed, as depicted in Fig. 7b.

### Possible mechanism of nanoflower formation

Based on our experimental findings, we propose a plausible mechanism for the formation of $WO_3$ nanoflowers *via* anodization (Fig. 8). Owing to the high oxidation potential of $W/W^{+6}$ (0.09 V *vs.* NHE) at STP, the process could be promoted in strong acid ($HNO_3$) to provide a highly oxidizing environment. In this study, nitric acid, which is known for its strong oxidizing properties, particularly at elevated temperature, was employed as the electrolyte for conducting these experiments.

In this study, $WO_3$ nanostructures were produced under optimized conditions, where the ultimate morphology of either the nanoflower-type or nanosheet was highly dependent on switching the experimental conditions. Two types of morphologies (nanosheets and nanoflowers) were obtained for anodic $WO_3$ under strong acid conditions. Based on literature and experimental conditions, we propose that the overall growth process follows three key stages. First, the oxidation of the W ($W/W^{n+}$, eqn (1)) sheet under anodic conditions is followed by oxidation of water and ionic dissociation of $HNO_3$ towards the formation of anions ($OH^-$, $O_2$, $NO_3^-$) in the electrolyte (eqn (2)). However, in this case, since W is also active, it competes with water oxidation, forming $WO_3$ (eqn (3)). In the last step, anions and cations ($W^{n+}$) are produced owing to the applied potential and coulombic attractive forces. The last step generally takes place at the electrode/electrolyte interface, where anions defuse from the electrolyte towards the anode due to the concentration and pH gradient, where they react with $W^{n+}$ cations to initiate the nucleation process. It is well-known that the diffusion of anions towards the anode depends on their reduction potential. Thus, there is a great chance that superoxide ions ($O^{2-}$) diffuse more readily towards the anode owing to their strong reducing ability.[33] Therefore, under static anodic conditions (15 V,

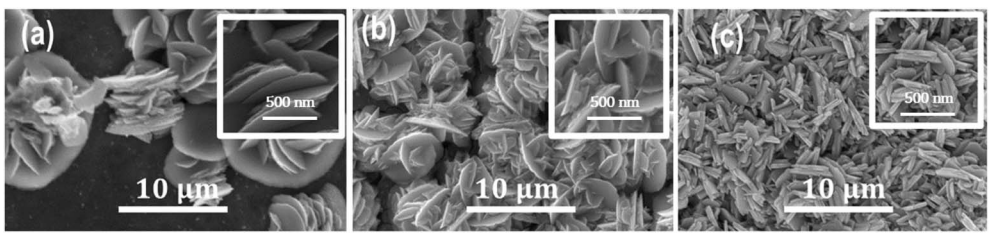


Fig. 6 Top surface FESEM morphology of $WO_3$ nanoflowers obtained at 15 V for 15 min and at 90 °C at various $HNO_3$ electrolyte concentrations (a) 0.5, (b) 1.5 M, and (c) 3.0 M with high-magnification images in the inset.

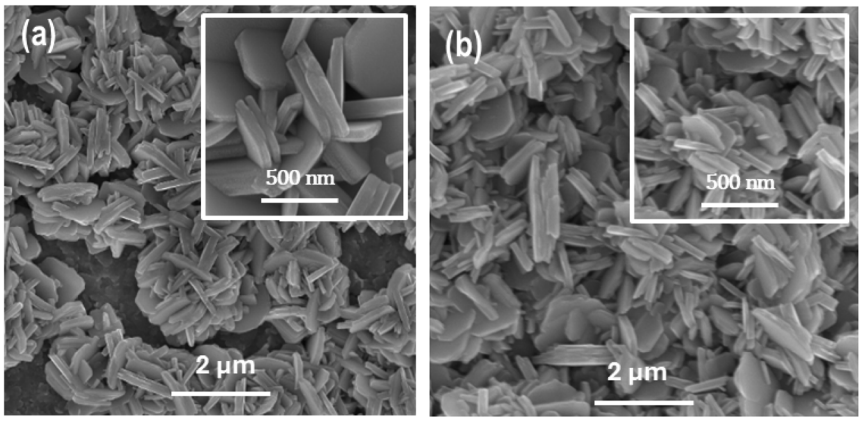


Fig. 7 Top surface FESEM morphology of $WO_3$ nanostructure obtained in 1.5 M $HNO_3$ at 15 V, 15 min, and 90 °C (a) without stirring and (b) with continuous stirring. The inset shows the high magnification images.

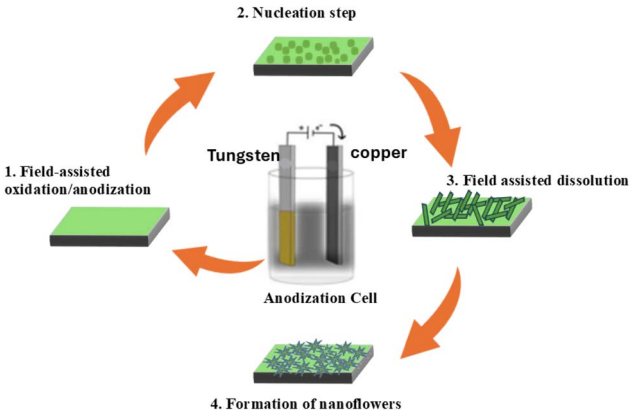


Fig. 8 The formation process of $WO_3$ nanoflowers on W sheet in $HNO_3$ based electrolyte *via* anodization.

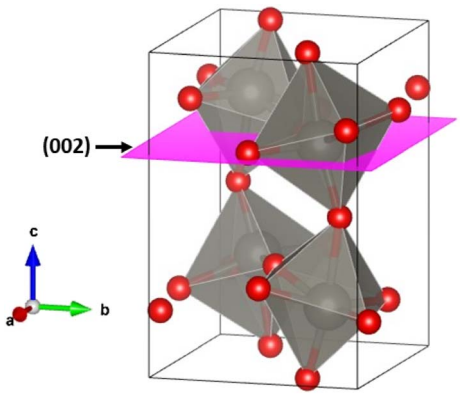


Fig. 9 Monoclinic $WO_3$ unit cell showing the (002) facet.

15 min, 90 °C, and 1.5 M), an uninterrupted reaction between anions and cations occurred at the $W^{n+}$/electrolyte surface, leading to the development of a nanoflower-like morphology. This flower-like morphology is probably due to the possible arrangement of the nanosheets with the lowest surface energy.[34]

$$W \rightarrow W^{6+} + 6e^- \quad (1)$$

$$2H_2O \rightarrow O_2(g) + 4H^+ + 4e^- \quad (2)$$

$$W(s) + 3H_2O \rightarrow WO_3 + 6H^+ + 6e^- \quad (3)$$

During a anodic potential, there is also the possibility of the formation of $WO_3$ ions at the surface of the anode owing to hydroxyl ions as a result of water ionization (eqn (4) and (5)).[33]

$$W^{6+} + 3O^{2-} \rightarrow WO_3 \quad (4)$$

$$W^{6+} + 3OH^- \rightarrow WO_3 + 3H^+ + 6e^- \quad (5)$$

Similarly, several other processes occur simultaneously to complete the entire mechanism. As previously discussed, water oxidation can be used to facilitate eqn (6) and (7) for long-lasting anodic processes while generating cations/anions. $WO_2^{2+}$ ions are unstable which form more stable $WO_3.H_2O$ liberates protons from the electrolyte (eqn (7)).

$$WO_3 + 2H^+ \rightarrow WO_2^{2+} + H_2O \quad (6)$$

$$WO_2^{2+} + 2H_2O \rightarrow WO_3.H_2O + 2H^+ \quad (7)$$

In addition, the nitrate ($NO_3^-$) ions present in the electrolyte also participate in the process and form unstable tungstate ($WO_4^{2-}$) ions during the field-assisted dissolution mechanism, which is unstable and forms more stable $WO_3 \cdot H_2O$ with $H^+$, as shown in eqn (8) and (9), respectively: tungstate ions can also combine with $OH^-$ ions to form tungsten hydroxide that precipitates upon saturation and initiates the formation of nanoflowers and nanosheet-like morphology (eqn (10)).[34]

$$2NO_3^- + WO_3 + H_2O \rightarrow WO_4^{2-} + 2HNO_2 \quad (8)$$

$$WO_4^{2-} + 2H^+ \rightarrow WO_3 \cdot H_2O \quad (9)$$

$$WO_4^{2-} + 2OH^- \rightarrow WO_3.(OH)_2^{2-} \quad (10)$$

The development of appropriate morphology involves nucleation and growth. We believe that *in situ* generated tungstate ($WO_4^{2-}$) ions initially precipitate on the surface of the W sheet and act as nuclei.[35] Nuclei are usually initiated at the grain boundaries of the W sheet due to high energy zones. As the anodizing time increased, the nuclei tended to reduce their surface energy by aggregating in the form of nanosheets *via* Ostwald ripening phenomenon.[36] Over time, we observed that the nanoplates were assembled and achieved a nanoflower-like morphology. From this, we can deduce that due to the high surface energy of the initial nuclei and fast precipitation of the starting layer in the form of nanoplates, the remaining continuously deposited materials compete in a limited space within the initial precipitation.[37] Consequently, most of the nanoplates are forced to grow perpendicularly, resulting in a densely packed flower-shaped structure, and these nanosheets from different sides come together to form an inter-connected network structure. Upon annealing, tungsten hydroxide in air at 450 °C for 1 hour, the monoclinic form of tungsten oxide was formed. This was attributed to the removal of the water trapped during anodization. It is evident from the diffractogram that monoclinic $WO_3$ was produced after annealing. The (002) facet is the most dominant plane and appears with the highest intensity. Therefore, it is concluded that this is a high-energy plane, and crystal growth occurs through this plane-forming nanosheet and finally nanoflower morphology. The monoclinic unit cell of $WO_3$ with the (002) plane is shown in Fig. 9.

By employing the proposed mechanism, it became apparent that the applied potential starts the nucleation process of the nanoplates. The applied potential primarily accelerated the reactions described in eqn (1) and (2), consequently generating a large quantity of readily soluble species available for precipitation. Conversely, it did not influence the reaction described in eqn (4), which governs the growth of the nanostructured film.[37]

## Conclusion

$WO_3$ nanostructures with nanoflowers and nanosheets morphologies were successfully obtained using a facile and simple anodization technique in $HNO_3$ aqueous electrolyte. This study systematically explored the effects of anodizing time, temperature, electrolyte concentration, and stirring on the evolution of $WO_3$ nanostructures morphology. A clear correlation was established, revealing that specific conditions drove the formation of nanoflowers and nanosheet structures. We present a possible mechanism for the formation of nanoflowers under specific conditions and their conversion into nanosheets. These findings provide valuable insights into optimizing $WO_3$ nanostructures for tailored applications and serve as a foundation for future research on the anodization of $WO_3$ in nitric acid.

## Data availability

The data supporting this article have been included in the main text of the manuscript.

## Author contributions

Rizwana Ghazi conducted experimental work and drafted the original manuscript. Dr Habib Ullah helped in the characterization, Dr Ghafar Ali conceptualized the research, performed the formal analyses and supervised the work. Prof. Zia ur Rehman reviews and edits the manuscript with useful input and insight. Dr Sajid Iqbal executed the data analyses and characterizations, while Dr Maaz Khan and Dr S. H. M. contributed to the interpretation of results and reviews. Prof. Jong-Il Yun and Prof. Sung Oh Cho assisted with the review and editing process with financial support.

## Conflicts of interest

The authors declare that they have no known competing financial interests or personal relationships that could influence the work reported in this study.

## Acknowledgements

This work was supported by the Korea Institute of Energy Technology Evaluation and Planning (KETEP) grant funded by the Korean Government Ministry of Trade, Industry, and Energy (RS-2023-00236697).

## References

1 G. Ali, Y. J. Park, A. Hussain and S. O. Cho, *Nanotechnology*, 2019, **30**, 095601.
2 M. O. Besenhard, A. P. LaGrow, A. Hodzic, M. Kriechbaum, L. Panariello, G. Bais, K. Loizou, S. Damilos, M. M. Cruz and N. T. K. Thanh, *Chem. Eng. J.*, 2020, **399**, 125740.
3 M. Salvador, G. Gutiérrez, S. Noriega, A. Moyano, M. C. Blanco-López and M. Matos, *Int. J. Mol. Sci.*, 2021, **22**, 427.
4 A. Nandagudi, S. H. Nagarajarao, M. S. Santosh, B. M. Basavaraja, S. J. Malode, R. J. Mascarenhas and N. P. Shetti, *Mater. Today Sustain.*, 2022, **19**, 100214.
5 W. Ahmed, S. N. Kazi, Z. Z. Chowdhury, M. R. B. Johan, S. Mehmood, M. E. M. Soudagar, M. A. Mujtaba, M. Gul and M. S. Ahmad, *Renewable Sustainable Energy Rev.*, 2021, **145**, 111025.
6 M. Parashar, V. K. Shukla and R. Singh, *J. Mater. Sci.: Mater. Electron.*, 2020, **31**, 3729–3749.
7 Z. Su and W. Zhou, *J. Mater. Chem.*, 2011, **21**, 8955–8970.
8 M. Paz Martínez-Viademonte, S. T. Abrahami, T. Hack, M. Burchardt and H. Terryn, *Coatings*, 2020, **10**, 1106.
9 E. Fazio, S. Spadaro, C. Corsaro, G. Neri, S. G. Leonardi, F. Neri, N. Lavanya, C. Sekar, N. Donato and G. Neri, *Sensors*, 2021, **21**, 2494.
10 M.-M. Zhang, J.-Y. Chen, H. Li and C.-R. Wang, *Rare Met.*, 2021, **40**, 249–271.
11 J. S. Santos, P. d. S. Araujo, Y. B. Pissolitto, P. P. Lopes, A. P. Simon, M. d. S. Sikora and F. Trivinho-Strixino, *Materials*, 2021, **14**, 383.

12 N. Gao, J. Cao, C. Wang, Z. Gao, R. Li, G. Ding, H. Ma, Y. Wang and L. Zhang, *Langmuir*, 2021, **38**, 164–173.
13 F. Keller, M. S. Hunter and D. L. Robinson, *J. Electrochem. Soc.*, 1953, **100**, 411.
14 G. Ali and M. Maqbool, *Mater. Chem. Phys.*, 2019, **233**, 21–26.
15 D. O. Miles, P. J. Cameron and D. Mattia, *J. Mater. Chem. A*, 2015, **3**, 17569–17577.
16 A. C. V. Bianchin, G. R. Maldaner, L. T. Fuhr, L. V. R. Beltrami, C. d. F. Malfatti, E. S. Rieder, S. R. Kunst and C. T. Oliveira, *Mater. Res.*, 2017, **20**, 1010–1023.
17 R. Hang, F. Zhao, X. Yao, B. Tang and P. K. Chu, *Appl. Surf. Sci.*, 2020, **517**, 146118.
18 J. Ou, M. Ahmad, K. Latham, K. Kalantar-Zadeh, G. Sberveglieri and W. Wlodarski, *Procedia Eng.*, 2011, **25**, 247–251.
19 A. Mozalev, Z. Pytlicek, K. Kamnev, J. Prasek, F. Gispert-Guirado and E. Llobet, *Mater. Chem. Front.*, 2021, **5**, 1917–1931.
20 L. Fang, L.-W. Bai, D. Wu, H.-T. Che, Y. Jiang, Y. Wang, H. Dong and F.-M. Zhang, *Chem. Eng. J.*, 2025, **510**, 161820.
21 H. Dong, L. Fang, K.-X. Chen, J.-X. Wei, J.-X. Li, X. Qiao, Y. Wang, F.-M. Zhang and Y.-Q. Lan, *Angew. Chem., Int. Ed.*, 2025, **64**, e202414287.
22 X. Li, S. Lin, R. Hu, P. Liang, Q. Wu, B. Yang, S. Lin, Q. Xu, J. Mei and J. Zou, *J. Opt. Photon. Res.*, 2025, 1–21.
23 N. Mukherjee, M. Paulose, O. K. Varghese, G. K. Mor and C. A. Grimes, *J. Mater. Res.*, 2003, **18**, 2296–2299.
24 Y.-C. Nah, A. Ghicov, D. Kim and P. Schmuki, *Electrochem. Commun.*, 2008, **10**, 1777–1780.
25 H. Tsuchiya, J. M. Macak, I. Sieber, L. Taveira, A. Ghicov, K. Sirotna and P. Schmuki, *Electrochem. Commun.*, 2005, **7**, 295–298.
26 T. Zhang, M. Paulose, R. Neupane, L. A. Schaffer, D. B. Rana, J. Su, L. Guo and O. K. Varghese, *Sol. Energy Mater. Sol. Cells*, 2020, **209**, 110472.
27 T. Kikuchi, J. Kawashima, S. Natsui and R. O. Suzuki, *Appl. Surf. Sci.*, 2017, **422**, 130–137.
28 M. Zych, K. Syrek, L. Zaraska and G. D. Sulka, *Molecules*, 2020, **25**, 2916.
29 K. K. Upadhyay, M. Altomare, S. Eugénio, P. Schmuki, T. M. Silva and M. F. Montemor, *Electrochim. Acta*, 2017, **232**, 192–201.
30 M. B. Rahmani, M. H. Yaacob and Y. M. Sabri, *Sens. Actuators, B*, 2017, **251**, 57–64.
31 E. Widenkvist, R. A. Quinlan, B. C. Holloway, H. Grennberg and U. Jansson, *Cryst. Growth Des.*, 2008, **8**, 3750–3753.
32 N. Khaliq, G. Ali, M. A. Rasheed, M. Khan, Y. Xie, P. Schmuki, S. O. Cho and S. Karim, *Nanoscale*, 2024, **16**, 12207–12227.
33 G. Ali, Y. J. Park, A. Hussain and S. O. Cho, *J Nanotechnology*, 2019, **30**, 095601.
34 Y. Chai, I. K. Chin, F. K. Yam and Z. Hassan, *J. Electrochem. Soc.*, 2014, **161**, 202.
35 M. Anik and O. Asare, *J. Electrochem. Soc.*, 2002, **149**, B224.
36 S. S. Golia, C. Puri, R. A. Zargar and M. Arora, *Metal Oxide Nanocomposite Thin Films for Optoelectronic Device Applications*, 2023, pp. 1–44.
37 E. Widenkvist, R. A. Quinlan, B. C. Holloway, H. Grennberg and U. Jansson, *Cryst. Growth Des.*, 2008, **8**, 3750–3753.